





Coupled Modeling and Fusion Control for a Multi-modal Deformable Land-air Robot

Xinyu Zhang , *Member, IEEE*, Yuanhao Huang , *Graduate Student Member, IEEE*, Kangyao Huang , Ziqi Zhao, Jingwei Li, Huaping Liu , *Senior Member, IEEE*, and Jun Li

Abstract—This paper introduces a structure-deformable land-air robot which possesses both excellent ground driving and flying ability, with smooth switching mechanism between two modes. The elaborate coupled dynamics model of the proposed robot is established, including rotors, chassis, especially the deformable structures. Furthermore, taking fusion locomotion and complex near-ground situations into consideration, a model based controller is designed for landing and mode switching under various harsh conditions, in which we realise the cooperation between fused two motion modes. The entire system is implemented in ADAMS/Simulink simulation and in practical. We conduct experiments under various complex scenarios. The results show our robot can accomplish land-air switching swiftly and smoothly, and the designed controller can effectively improve the landing flexibility and reliability.

Index Terms—Coupled dynamic modeling, land-air robot, smooth multi-modal switch, jerk limited trajectory, fusion control.

I. INTRODUCTION

ROBOTS are commonly used in rescue and searching due to their safety. As an important branch of robotics, aerial robotics can provide stable, fast and reliable remote sensing information at high altitudes thanks to their convenience and flexibility [1], [2]. Single locomotion robots often struggle to adapt in highly variable or uncertain environments. Land-air robots offer both flying and driving capabilities for increasing spatial flexibility as well as reducing the energy demands of continuous flight.

One typical category is the hybrid terrestrial and aerial quadrotor [3]–[5]. These robots are generally composed of a quadrotor hinged at the center of a cylindrical cage or a pair of coaxial passive wheels. The terrestrial moving depends on the aerodynamics power generated by rotors. But the downwash effect by rotors may cause reduction of perception capability while driving [6]. Another class of robots have both active aerial and terrestrial moving ability, which require driving or walking base [7]. For instance, a robot utilizes suckers attached to legs to adsorb on the surface for bridge inspection and

maintenance [8]; drivocopter by Jet Propulsion Lab uses four oblate spherical shape elastic cages as wheels to protect the propellers and absorb shock forces while landing [9]. Besides, chassis is widely used in multi-modal robots design to enhance the ground moving performance [10]–[12].

Deformable robots can adjust the structures to environments. In general, rotorcrafts usually demand larger propeller blade area for higher lifting force which can be obtained by increasing the number of rotors or lengthening the propellers' size. Driving on ground nevertheless prefers smaller and more flexible base for better trafficability, especially passing through the narrow and unstructured environment. Conflict of the space utilization occurs among multi-modes consequently. To tackle this, the design of structural reuse and deformable structure is the mainstream. In addition to sharing actuators, flying star can adjust body height via a servo motor, to through a tunnel [13]. In [14], robot is able to shrink its coaxial rotors adhere to the body, and can overcome most of obstacles. Similar concept appears in [15], the propellers protection is modified to wheel-shaped structure. Robot can transform between terrestrial and aerial locomotion directly driven by servos.

In addition, the robot needs to ensure stability and smoothness during switching motion modes. The robot in this study can be regarded as a coupled aircraft and chassis. Proportional–Integral–Derivative (PID) [16], Nonlinear Model Predictive Control (NMPC) [17], reinforcement learning (RL) [18], and other methods or controllers can perform single-mode stable control of the robot. It can also plan the trajectory by EGO-Planner [19], Jerk Limited Trajectory (JLT) [20] and so on. Generally speaking, external disturbances and main actuators usually switch as the environment changes. The impact of the ground and the ground effect will cause influent the robot at the moment of mode switching. These problems will bring huge challenges to the mode switching control of land-air robots [21].

In previous works, we developed the multi-modal robot with hexacopter and focused on the continuous landing control based on a MPC controller [7]. On this basis, deforma-structure land-air prototype is also introduced in [22] and its detailed structure is shown in Fig.1. This paper further introduced the details of this robot including the mechatronics, modeling, as well as the control. We designed controller for the mode-switching tasks considering strict scenarios and disturbance. The contributions of this paper are summarized as follows:

- We introduce an innovative structure and mechatronics design of variable-structure land-air robots, including

Xinyu Zhang, Ziqi Zhao, Jingwei Li, Jun Li are with the School of Vehicle and Mobility, Tsinghua University, Beijing, P.R.China (e-mail: xzyzhang@tsinghua.edu.cn; 273456@whut.edu.cn; lijw00123@163.com; lj19580324@126.com)

Yuanhao Huang is with the School of Vehicle and Mobility, Tsinghua University, Beijing, P.R.China, and also with the School of Aviation, Inner Mongolia University of Technology, Hohhot, Inner Mongolia, P.R.China (e-mail: huangyuanhao_work@163.com)

Kangyao Huang and Huaping Liu are with the Department of Computer Science and Technology, Tsinghua University, Beijing, P.R.China (e-mail: kangyao.huang@outlook.com; hpliu@tsinghua.edu.cn)

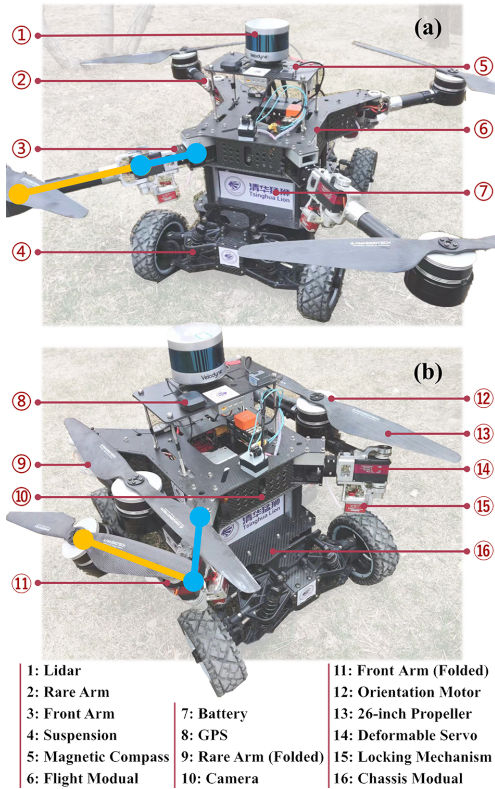


Fig. 1. The overall structure design of the robot. (a) When the arms are deployed, the robot obtain a large pulling force and load capacity with the 26-inch propeller. (b) After the arms are folded, robot’s driving flexibility and passage capacity are improved.

folding arms, locking mechanisms and the motor for fixed propeller.

- A coupled dynamics model is proposed to describe the multi-modal motion of land-air robots. Meanwhile, the deformable structure is analyzed to ensure the robot’s reliability.
- Combined with the robot dynamics model and ground effect model, this study proposed a fusion controller based on LQR and JLT for the continuous take-off and landing tasks of land-air robots in slope scenes. The simulation and experiments provides strong evidences of the effectiveness and robustness.

The remainder of the article is organized as follows. Section II describe the specific design of the robot, including novel structures and mechatronics. Section III reports the details kinematic and dynamics model. Section IV Presents the results of simulations and experiments. Section V concludes the work.

II. MECHATRONICS DESIGN

The design of the robot depends on its operating context. To balance the robot’s ability in multi-modal scenarios, we cannot simply combine the quadrotor with the chassis. The energy-system analysis, power-system selection, and lightweight design improved the robot’s duration time. The robot also reduces weight by sharing energy systems and control systems. Meanwhile, relying on deformable structure design ensures the robot’s mighty flight power and flexible ground moving

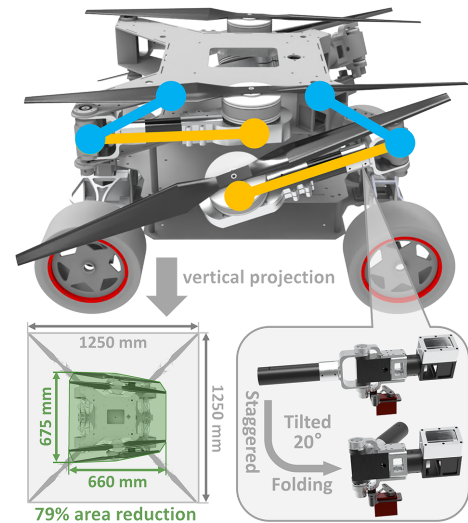


Fig. 2. Self-deforming structures are an innovative approach to balancing land-air robots’ flying and driving capabilities. The blue lines mean the fixed arms, and the yellow lines mean the folding arms. The staggering folding method reserves the large-sized propellers and keeps the robot minimized and stable movement in driving mode.

state. In this section, we mainly introduced the analysis and design of the deformable structures and mechatronics. The key parameters shown in Tab.I are used in the high-fidelity model building.

TABLE I
SPECIFICATION OF THE ROBOT.

Height	Body	552 mm
Weight	Total (exclude payload)	20.62 kg
	Battery	5.74 kg
	Flight Module	7.81 kg
	Chassis	7.07 kg
Speed	Max Flying Speed	7.47 m/s
	Max Driving Speed	15.10 m/s
Flight Module	Flight Motor	5 Nm
	Kv Value	170
	Propeller	26 inch
	Steering Gear	8 Nm
Chassis	Kv Value	800
	Driving Motor	12 Nm

Our power-system uses 26-inch propellers for more pulling power. However, in the flying mode, the robot assumes a standard quadrotor configuration with a maximum length and width of 1250 mm. The huge size makes it difficult to pass through complex unstructured scenes such as outdoors and indoors. In addition, the scattered mass distribution leads to reduced dynamic stability and vibration of the robot [23]. Therefore, a deformable structure is required to reduce the size when moving on the ground. Fig.2 shows this staggered folding strategy. The platform enters the driving mode when the steering gear drives the four arms to rotate independently. The robot’s front arms are tilted by 20 degrees, and the rear arms are horizontal. The design avoids the arms’ collisions and further reduces the robot’s size. At this time, the vertical projection area of the robot is reduced by 79% compared with the flying mode. The robot’s size, limited to 700mm, can easily

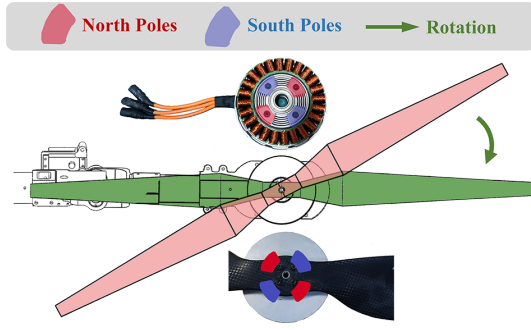


Fig. 3. The motor limits the propeller's orientation by the non-contact magnet's position. After receiving a collision or artificially moving the propeller, it only takes 1-2 s to restore the position quickly.

navigate through narrow passages or gates. Furthermore, the deformable arms are driven by servos directly. Herein, we design a locking-mechanism as the last line of flying safety.

When driving on the land, rotors should keep propellers and arms in the same orientation to avoid collisions between the propeller and the body (Fig.3). Relying on mechanical or electrical stops may increase system complexity, so a magnet mechanism is introduced to keep propellers position. The magnet can generate attractive force without contact and is used for fixation and restraint [24]. Here, four magnets with different polarities are staggered on the inner and outer of the motor as a passive positioning mechanism. The magnets are distributed up and down without contact, which reduce the motors power loss. In this way, magnets can keep the propellers a static state and quickly return to the favorable position in the case of rotation or offset.

Meanwhile, we use a mode switching controller to control the auto-folding and auto-locking mechanisms. The flight module has 8 servos to drive and lock the deformable arms. Four of servos are dual-axis steering gears for the automatic folding degree of freedom control, and the other four are locking servos are used to insert the fixed pin into the locking pin. The servo controller is equipped with a potentiometer array for fine-tuning servos, which can fine-tune eight servo positions. The potentiometer array fine-tunes the servo's po-

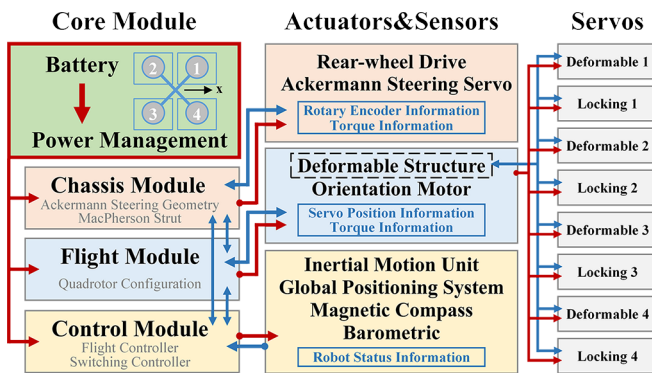


Fig. 4. Overview of the hardware system. The red lines represent power supply, and the blue lines represent signal communication. The flight and chassis modules of the robot share the power supply and controller. The serial number of each arm is shown in figure. From flight to driving mode, the robot must fold the rear arms first and then fold the front arms. Otherwise, unfold the front arm first and then the rear arm.

sition to reduce the gap created, causing by fit tolerance. The hardware system is shown in Fig. 4. This method effectively reduces the calculation pressure of the flight control and makes the flight safer.

III. KINEMATIC AND DYNAMICS MODEL

A. Kinematic Model

The land-air robot has a chassis module fixed connection to the flight module. Motors provide force and torque and the chassis with Rear-wheel drives and Macpherson Strut provide ground propulsion. Meanwhile, the land-air platform is a strongly coupled system with multiple degrees of freedom. To research the control algorithm of its movement during motion and modes switching, we should rely on the variable pose relationship of the model. The overall model of the land and air platform is in Fig.5. Considering the moment of inertia and fusion control during the movement process, we first made several assumptions for the model as follows.

- The connection between the frame of the rotor mechanism and the chassis is rigid and symmetrical.
- The four propellers are rigid and have no blade flapping.
- Assuming that the arm is rigid during flight and surface movement.

To accurately describe the relative pose relationship of the land-air platform, we defined body coordinate system ($CG - xyz$) and global coordinate system ($O_N - XYZ$). Creating the coordinate systems $\omega_n = [\phi \ \theta \ \psi]^T$ and $\omega_b = [p \ q \ r]^T$ according to the right-hand rule. Among them, ϕ , θ and ψ represent the roll angle, pitch angle and yaw angle of the body relative to the global coordinate system. And p , q and r represent the roll, pitch and yaw angular velocities of the body relative to the body coordinates, respectively.

Similar to [25], defines the position of the body's center of gravity in the global coordinate system as \vec{r}_n , the acceleration of the land-air platform in the global coordinate system as $\vec{F} = m\ddot{\vec{r}}$, the angular velocity of the body in the body coordinate system as $\vec{\omega}_b = [\dot{p} \ \dot{q} \ \dot{r}]^T$, and angular velocity in global coordinate system $\vec{\omega}_n = [\dot{\phi} \ \dot{\theta} \ \dot{\psi}]^T$.

The transformation matrix from the body coordinate system to the global coordinate system can express as nT_b .

The force defined in the body coordinate system ($CG - xyz$) can transform into the global coordinate system ($O_N - XYZ$) by the transformation matrix.

The transformation matrix of angular velocity nD_b from body coordinate to global coordinate can be denoted as

$${}^nD_b = \begin{bmatrix} 1 & S_\phi T_\theta & C_\phi T_\theta \\ 0 & C_\phi & -S_\phi \\ 0 & S_\phi / C_\theta & C_\phi / C_\theta \end{bmatrix} \quad (1)$$

where C represents \cos , S represents \sin and T represents \tan . The rotation equation of the flight module in the body coordinate system is

$$J_b \cdot \frac{d\vec{\omega}_b}{dt} = \vec{M}_b - \vec{\omega}_b \times J_b \cdot \vec{\omega}_b \quad (2)$$

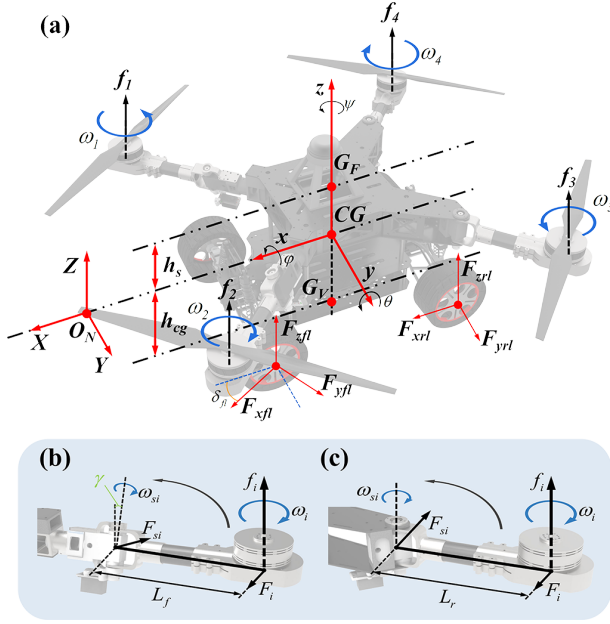


Fig. 5. Setting of Equivalent Mathematical Model of Land-Air Robot.(a) Modeling of the Overall System and Flight Module. (b) and (c) Modeling of the folding part of the front and rear arms.

where \vec{M}_b is the total torque of the system, J_b is the rotational inertia matrix of the flight module in the body coordinate system, M_g is the torque generated by the gyroscopic effect, and M_d is the torque generated by aerodynamic friction. By estimating the transformation matrix nD_b , the fixed coordinate system of the flight module body transfers the angular acceleration into the global coordinate system. To simplify the model, assume that the inertia matrix J_b is a diagonal matrix.

$$J_b = \text{diag}[J_x, J_y, J_z] \quad (3)$$

Two submodels are analysed in the following subsections to calculate the forces and moments acting on the flight module and perform further analysis.

B. Flight Module Dynamic Model

This section established an equivalent dynamic model of the flight module. The quadrotor is a lacks coupled rigid body model with six degrees of freedom, similar to the Fig.5(a). According to the Newton-Euler equation, the dynamic model of the quadrotor aircraft can be denoted as

$$M_b = J_b \dot{\omega}_b + \omega_b \times J_b \omega_b + M_g + M_d \quad (4)$$

The synthesis of gyroscopic effect torque M_g and aerodynamic friction torque M_d can be denoted as

$$M_g = \sum_{i=1}^4 \vec{\omega}_b \times J_b [0 \quad 0 \quad (-1)^{i+1} \Omega_i]^T \quad (5)$$

$$M_d = \text{diag}(d_\phi, d_\theta, d_\psi) \dot{\zeta} \quad (6)$$

where $J_b = \text{diag}(d_\phi, d_\theta, d_\psi)$ is the moment of inertia of each rotor. d_ϕ , d_θ and d_ψ is the corresponding aerodynamic damping coefficient.

The translation equation of the quadrotor aircraft in the global coordinate system can be derived

$$m\ddot{P} = {}^nD_b \cdot F + \begin{bmatrix} 0 \\ 0 \\ -mg \end{bmatrix} - \begin{bmatrix} d_x \dot{x} \\ d_y \dot{y} \\ d_z \dot{z} \end{bmatrix} \quad (7)$$

where d_x , d_y and d_z are respectively represent the introduced aerodynamic friction coefficient, which use to calculate the resistance of translational motion, and F is the lift generated by the rotor to the flight module.

Complex deformable arms can affect the payload and reliability of the land-air robot. Each rotor is fixedly connected to the main body of the land-air robot by an independent arm. The steering machines in each arm enable the rotor to rotate independently about the main body. In the dynamic modelling process of the arms are approximated as rectangular cuboids [26]. The propeller will generate yaw force during rotation, relying on the force generated by the steering gear to maintain the fuselage structure5(b) and (c). The moment of inertia of the arm can be denoted as

$$J_{fi} = \frac{m_i}{12} L_{fi}^2 \cdot \cos(\gamma) \cdot (w_{si}^2 + L_f^2) \quad (8)$$

$$J_{ri} = \frac{m_i}{12} L_{ri}^2 \cdot (w_{si}^2 + L_f^2)$$

where m_i is the mass of the arm, J_i is the moment of inertia of the arm around the axis of the steering gear. When the propeller is stationary, the force F_{si} at the front arm deformation actuator is only the component force of gravity. When the propeller rotates, the force is the resultant force of yaw moment F_i and gravity in the radial direction of the rotating shaft. The dynamic equation of the deformable arm is

$$\text{diag}(m_i) \begin{bmatrix} \ddot{x} \\ \ddot{y} \\ \ddot{z} \end{bmatrix} = \begin{bmatrix} F_{xi} \\ F_{yi} \\ F_{zi} \end{bmatrix} \quad (9)$$

F_{xi} , F_{yi} and F_{zi} ($i = 1 \dots 4$) are the decoupling forces along the axis, the axis and the z-axis at the rotating shaft of each motor, respectively, and the rotation matrix decouple the torque.

The reference coordinate is the global coordinate system. When the arm and the rotor rotate relative to the land-air platform, the inertia tensor of the arm will not rotate. The inertia tensor of the arm can be denoted as

$$J_{arm,i} = R_z(\theta_i) J_{arm} R_z(\theta_i)^T \quad (10)$$

where R_z is the rotation matrix around the z-axis(θ_i) of the global coordinate system, $i = (fl, fr, rl, rr)$. The moment of inertia of the motor does not change when it rotates around its z-axis. The rotation can be ignored for the moment of inertia of the motor and rotor. So that the steering gear joint can be regarded as a rigid body during flight and ground movement.

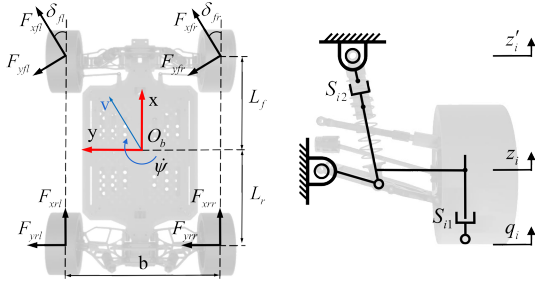


Fig. 6. Mathematical modeling of Ackerman chassis and MacPherson suspension.

According to the equation(2), the rotation equation of the aircraft dynamics model can be denoted in the body coordinate system as

$$\begin{bmatrix} \dot{p} \\ \dot{q} \\ \dot{r} \end{bmatrix} = \begin{bmatrix} [-d_x \cdot l \cdot p + F_x + qr(J_y - J_z)]/J_x \\ [-d_y \cdot l \cdot q + F_y + pr(J_z - J_x)]/J_y \\ [-d_z \cdot l \cdot r + F_z + pq(J_x - J_y)]/J_z \end{bmatrix} \quad (11)$$

J_x , J_y and J_z are the moments of inertia around the x-axes, y-axes, and z-axes in the corresponding directions, respectively. F_x , F_y and F_z represent the force of the actuator, respectively. The relationship of the force and the torque can be denoted as

$$\begin{bmatrix} F \\ F_x \\ F_y \\ F_z \end{bmatrix}^T = c_\Omega \cdot M_4 \cdot \sum_{i=1}^4 \omega_i^T \quad (12)$$

c_Ω is the thrust coefficient, $\alpha = 45^\circ$ is half of the angle between the arms of the quadrotor, $\omega_i (i = 1 \dots 4)$ is the rotational speed of the rotor, and M_4 is the control matrix of the quadrotor, which can be denoted as a normal quadrotor.

C. Chassis Dynamic Model

This paper uses the magic formula [27] to describe the tire. The tire model is subjected to longitudinal force to maintain the speed, and the following equation approximates the lateral force

$$lF_{yi} = D_L \cdot \sin[C_L \cdot \arctan\{B_L \alpha_i - E_L(B_L \alpha_i - \arctan(B_L \alpha_i))\}] \quad (13)$$

where $i = (fl, fr, rl, rr)$, B_L , C_L , D_L and E_L are the parameters obtained by modelling fitting. z_i represents the vertical displacement of the wheel, and the longitudinal load F_{Ni} can be denoted as

$$F_{Ni} = m_i \ddot{z}_i + c_i (\dot{z}_i - \dot{z}'_i) + k_i (z_i - z'_i) \quad (14)$$

where \dot{z}'_i represents the vertical displacement of the spring end point of the wheel.

$$F_{yi} \leq \sqrt{(\mu F_{Ni})^2 - F_{xi}^2} \quad (15)$$

After modelling the wheel, combine the results with the chassis model. Fig.6 shows the dynamic response of the chassis structure under force and moment. The translation

equation of the chassis in the x and y directions and the rotation equation in the yaw direction can be obtained by the following equations

$$\begin{cases} lM_b a_x = \sum_i F_{Li} - \frac{1}{2} \rho c_\omega A v_x^2 \\ M_b a_y = \sum_i F_{Qi} \\ J_z \ddot{\psi} = \frac{b}{2} (F_{Lfr} + F_{Lrr} - F_{Lfl} - F_{Lrl}) + \\ (F_{Qfl} + F_{Qfr}) \cdot L_f - (F_{Qrl} + F_{Qrr}) \cdot L_r + U_4 \end{cases} \quad (16)$$

where

$$\begin{aligned} F_{Li} &= F_{xi} \cos(\delta_i) - F_{yi} \sin(\delta_i) \\ F_{Qi} &= F_{xi} \sin(\delta_i) - F_{yi} \cos(\delta_i) \end{aligned} \quad (17)$$

The chassis's suspension system (Fig.6) is mainly consists of chassis (sprung mass, m'_i), suspension swing arm, shock absorber and wheels(unsprung mass, m_i). In the vertical direction, the sprung mass displacement is \dot{z}'_i , the unsprung mass displacement is \dot{z}_i , the ground disturbance is q_i . S_{i1} and S_{i2} represent the damping B_{i1} , B_{i2} and stiffness K_{i1} , K_{i1} of the shock absorber and the wheel, respectively.

The chassis suspension equation is established as follows:

$$\begin{cases} -K_{1i}(\dot{z}'_i - \dot{z}_i) - (B_{1i} + B_{2i})(\dot{z}'_i - \dot{z}_i) + f_a - f_d = m_i \ddot{z}'_i \\ K_{1i}(z_i - q_i) + K_{2i}(\dot{z}'_i - \dot{z}_i) + (B_{1i} + B_{2i})(\dot{z}'_i - \dot{z}_i) \\ -f_a = m_i \ddot{z}_i \end{cases} \quad (18)$$

where f_a and f_d represent actuator and disturbance forces, respectively. At this point, the state space of the suspension model can be denoted as:

$$\dot{X} = Ax + B_1 f_a + B_2 q_i + B_3 f_d \quad (19)$$

Where q_i represent the road disturbance.

IV. FUSION CONTROLLER DESIGN

Landing on the slope is a great challenge for the land-air robot, especially with a heavy coupled chassis. This section describes the algorithm for switching the robot's motion states with a finite state machine. Then, we considered the takeoff and landing process as an optimization problem. The fusion control of multi-modal motion is performed using the JLT-based trajectory planning controller and auxiliary controller described below. Meanwhile, the LQR-based auxiliary controller considers the modeling of ground effect. The whole motion and controller systems are shown in Fig.7.

A. Finite State Machine

Not only the robot's single-motion mode but multi-mode switching need to be carried out in different situations. The driving mechanism and control algorithm of multi-modal movement is also different. This paper relies on the finite state machine (FSM) to realize the control switching of the robot in multi-modal motion. The basic movements and control logic of the deformable structure are included in the FSM. We describe a common scenario for robot that divides state into

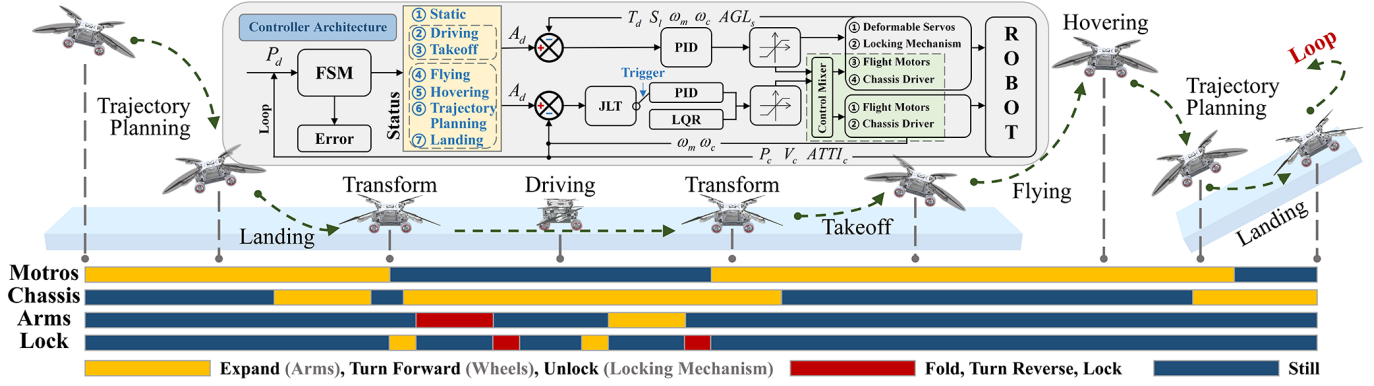


Fig. 7. The robot relies on the set finite state machine to switch between the motion state and the mode. Each actuator has a corresponding relationship with the motion state. The controller proposed in this paper is implemented based on JLT and LQR.

static, driving, transform, takeoff, flying, trajectory planning, and landing:

- *Static*: In this initial state, the robot is statically stable on the ground. The arms of the robot can be unfolded or folded. Then, the robot judges whether it reached the preset point to trick FSM switch to *Driving* or *Takeoff* states.
- *Transform*: In this state, the robot can deform its arms to transform to the different motion modes structure.
- *Drive*: The robot can drive on land in this state. If the arms were unfolded, the robot would unlock-fold-lock it immediately during motion. The robot will switch to the *Takeoff* state when it reaches the takeoff point.
- *Takeoff*: When the robot switch into this state, it will immediately unlock-unfold-lock the arms and prepare to fly. The robot can take off vertically or with a run-up. When the robot leaves the ground more than 500 mm, it can switch to the *Flying* state.
- *Flying*: In this state, the robot flies to the aim with the target point set. After reaching the present point, the FSM automatically switches to the *Hovering* state.
- *Hovering*: The robot keeps dynamic stability in this state. After reaching the hovering point, the robot can switch to the *TrajectoryPlanning* state.
- *Trajectory – Planning*: In this state, the robot plans its trajectory by the JLT-based controller in Section IV.B. After approaching the land, the robot automatically switches to the *Landing* state.
- *Landing*: In addition to the trajectory plan, the robot is also affected by ground effects when landing. The robot will rely on the LQR-based auxiliary controller (Section IV.C) for attitude stabilization in this state. The robot lands vertically or with a run-up and then can switch to *Static*, *Driving*, or *Takeoff* to make a loop.

B. Trajectory planning

This subsection proposes modeling and optimization methods for slope takeoff and landing scenarios.

Turning from air to a slope requires the robot to plan real-time according to the environment and is limited by the robot's dynamic constraints. Considering the strongly coupled

system and safety, the controller needs less computation and solid real-time performance. Meanwhile, taking off and landing on a slope requires precise control of the robot's trajectory, attitude (especial terminal posture), and speed. This study treats it as an optimization problem for its position, velocity and attitude. We follow [28] to assume that each axes can be denoted as a triple integrator. By solve the three spatial axes for independently and estimate the total cost to optimize [29]. Given a three differentiable motion $j(t)$, and the jerk can be denote as $\dot{j}_b = (\ddot{x}, \ddot{y}, \ddot{z})$.

To compute the thrice differentiable trajectory of the robot at the final time T . The cost function about jerk can denote as

$$\min(J_\Sigma) = \frac{1}{T} \int_0^T \|\dot{j}(t)\|^2 dt \quad (20)$$

subject to

$$\begin{aligned} 0 &\leq f_{\min} \leq f \leq f_{\max} \\ \|\omega\| &\leq \omega_{\max} \\ -v_{\max} &\leq v(t) \leq v_{\max}, \forall t \in [0, t_{\text{end}}] \\ -j_{\max} &\leq j(t) \leq j_{\max}, \forall t \in [0, t_{\text{end}}] \end{aligned} \quad (21)$$

The cost function can be interpreted as an upper bound on the average of a product of the inputs to the robot. f demonstrates the robot's flight thrust, which is limited by the fixed-pitch propellers. The angular velocity is limited into a ball by the dynamic model or sensors' saturation and denote a Euclidean norm $\|\omega\|$. The parameters above denote the input constraints and they work with the robot dynamics and motion constant to limit the cost function. Furthermore, the robot is fixed by two components of the parameters j and f . In this controller, the nonlinear model and the generation of the trajectory are simplified. The cost function can be decoupled into a per-axis cost j_k , which introduced the position, velocity and acceleration.

$$J_\Sigma = \sum_{k=1}^3 \frac{1}{T} \int_0^T \dot{j}_{k(p,v)}(t)^2 dt \quad (22)$$

where p, v are the each axis's position and velocity of robot, respectively. Define the components of the robot in each axis as

$$\kappa = [u(t), \dot{u}(t)] \quad (23)$$

Let T be the goal duration of the motive trajectory, and κ are the expected components at the end of the trajectory. The trajectory constraint of the expected components can be denoted as

$$\kappa_k(T) = \hat{\kappa}_k, (k = 1, \dots, 6) \quad (24)$$

To limit the desired position of the robot at the moment of mode switching to be as accurate as possible. And the speed can be kept within a specific range to ensure comfort during mode switching. Therefore, the optimal trajectory can be solved with $\hat{\kappa}$. If there are multiple generated trajectories, the trajectory cost can be calculated by the equation (20) to obtain the trajectory with the lowest cost.

C. Ground Effects and Motion Controller Design

Owing to the aerodynamic ground effect, the lift and pitching moment will increase. Significantly during takeoff and landing, the pitching moment can be increased by up to 60% [30], [31]. During the take-off and landing of the land-air robot on the slope, the disturbance of the attitude of the ground effect is particularly obvious. Because the robot cannot remain statically stable with a tilted attitude. These ground effect will cause instability in attitude and divergence of control. The equivalent ground effect model (EGEM) presented by [32] is efficient to describe the the ground effect. The model considers both altitude and forward velocity, and the velocity potential of source can be represented as

$$\phi = -\frac{(R/4z)^2}{\sqrt{(x-x_0)^2 + (y-y_0)^2 + (z-z_0)^2}} \quad (25)$$

The denote of the ratio of the thrust with ground effect and in air for single propeller is

$$\frac{T_{IGE}}{T_{OGE}} = \frac{1}{1 - \frac{(R/4z)^2}{1+(|V|/v_i)^2}} \quad (26)$$

where T_{IGE} and T_{OGE} denote the thrust of the robot in ground effect and out of ground effect, respectively. In addition to considering the effects of ground effects, the controller should also consider the wheels' and suspension metrics' dynamics model. Defined angular velocity $[\theta, \psi]^T$ and angular acceleration $[\dot{\theta}, \dot{\psi}]^T$ as Y_k . Linearizing and converting the chassis dynamics model to state space as

$$\begin{aligned} \dot{X}(t) &= AX + BU + G_d \\ Y(t) &= C_{out}X \end{aligned} \quad (27)$$

where the control input force on each motors is U and the influence of the ground effect and slack variables are G_d . The fusion controller triggers the switching of the controller through the height of the robot from the ground.

We considered the task as an infinite horizon optimal problem, and used a LQR-based controller to stabilize the robot and stable interference. The robot attitude is controlled

and optimized by minimizing the quadratic cost function as follow

$$\min(J_\Sigma) = \frac{1}{2} \int_{t_0}^{\infty} (Y^T Q Y + U^T R U + G^T T G + s^T P s) dt \quad (28)$$

subject to

$$\begin{aligned} Y_{\min} - s &\leq Y \leq Y_{\max} + s \\ G_{\min} - s &\leq G \leq G_{\max} + s \\ \Delta U_{\min} &\leq \Delta U \leq \Delta U_{\max} \\ 0 &\leq U \leq U_{\max} \\ s &\geq 0 \end{aligned} \quad (29)$$

In this part, slack variable s was introduced to make the cost function easily solve in a larger feasible region. The robot solves the optimal motion trajectory through equations (20 to 24), and the auxiliary controller assists in adjusting the posture before landing. Among them, the pitch angle at the moment of landing determines whether the landing on the slope is smooth and safe. Whether the yaw angle and the speed direction remain the same determines whether it is smoothly mode-switching from flight to wheel drive.

V. VALIDATION AND DISCUSSION

This subsection describes the validation of the robot by simulations. We built a detailed simulation model in ADAMS based on models in Section III and parameters in Tab.I; then we evaluated the fusion controller in Section IV. For comparison, we also built a parallel cascade PID controller during flight, ground travel, and structural deformation independently as a baseline. The controller generates rotational speed of each motor for flight control and chassis steering and wheel speed for ground motion.

A. Vibration test of robot ground driving

Foldable rotary mechanism can reduce the damage of arms and caused by vibration. In simulation, we tested the effects on robot vibration with and without the deformable structures. At the same time, the simulation of slope landing verifies the robust and validity of proposed fusion controller.

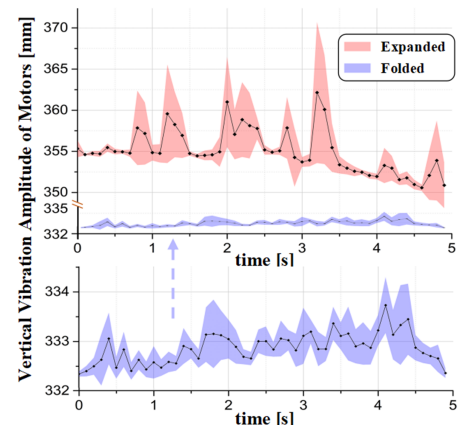


Fig. 8. Unstructured scene details for ground motion experiments.

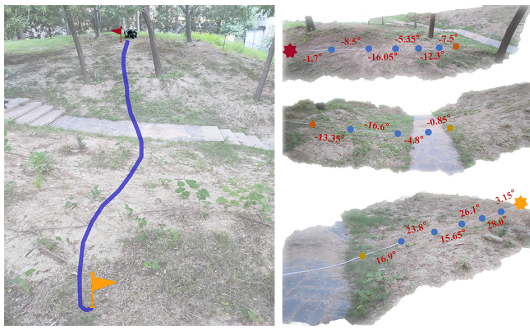


Fig. 9. Unstructured scene details for ground motion experiments.

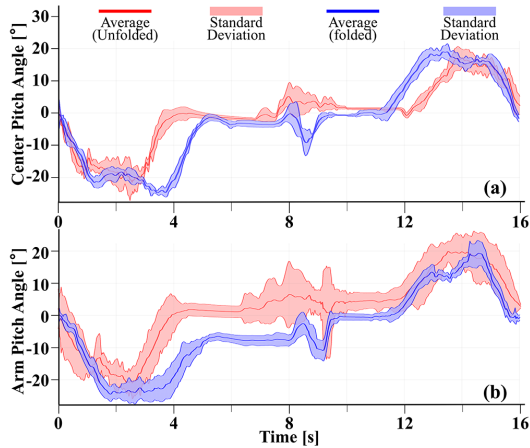


Fig. 10. The average and standard deviation of the angular transformation in different modes to observe the vibration.

1) *Simulation test:* In addition to changing the volume of the robot to pass through tight areas, the deformation mechanism can also reduce vibration caused by fit tolerance. Coupled with the movable structure and scattered mass distribution of the robot, the large amount of vibration generated when driving on the ground will cause irreversible damage to the mechanism.

To verify the optimization of the robot vibration before and after deformation, we take the average vertical displacement H of the four motors as a reference. Fig.8 show the error diagrams of the reference quantity H in the unfolded and folded states of the robot. When the robot arm unfolds, the ground driving will generate severe vibration and transmit it to the motor. It is caused by the outward extension of the arm, the deformable mechanism with large fit tolerance, and the extensive mass dynamic system and the maximum shaking displacement reaches 25mm. When the arm is folded, the vibration generated during driving is significantly reduced and the maximum is about 3mm.

2) *Field Experiments:* In this experiment, the robot is commanded to drive on a filed environment with steep slope up to 28° . The slope is shown in Fig.9, and we recorded the slope angle for each 1-m long segment for reference. Five inertial sensor modules (IMU) are mounted on the robot's places of center and four motors. By measuring the angle change of each key position of the robot to evaluated the vibration of the robot caused by the fit tolerance. Loss of control and ground slip

during movement in the wild are also our concerns [33]. And a global positioning system (GPS) system is mounted on the robot for the location.

The robot is commanded to drive 10 sets of experiments on the slope at a speed of 1 m/s in expending and folded modes and obtained 5 sets of valid experimental data, respectively. Fig.10shown the fitting results of the pose angles' changes of each critical position in two modes. Front arms, rare arms and center's average data are respectively shown as lines with the standard deviation shaded around the average. The robot maintained an excellent ground movement ability when it folded the arms. In the experimental comparison of unfolding and folding, unfolded arms caused greater amplitude and frequency vibrations. The resulting vibrations of the center position are closer between two motion modes. When the arms unfolded, the robot's speed was easily out of control and slipping at 3-5 seconds and 11-13 seconds. As such, the robot has more trajectory offsets and is difficult to control in the unfolding mode in the actual moving process.

B. Controlling test of robot ramp mode switching

The challenges of mode switching on slopes mainly focus on motion planning and adjusting speed and attitude before landing. The slope is usually no more than 10 degrees for general urban or roadway scenes. Furthermore, for rotor-driven robots, the 30-degree slope is also a challenging scenario to land or take off. If the land-air robot could perform flexible and compliant mode switching in these two scenarios, it could also perform tasks in more complex unstructured scenarios.

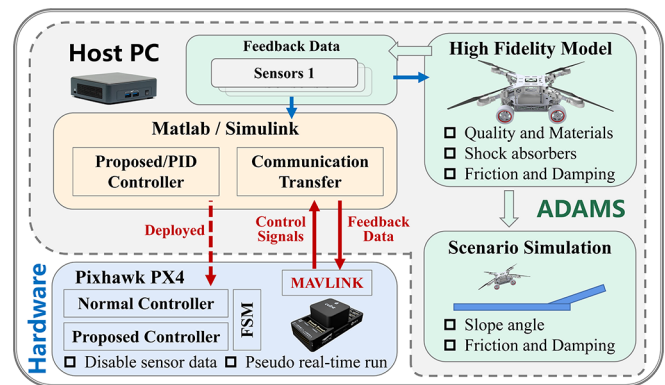


Fig. 11. The hardware-in-the-loop test platform. The control code was generated by Simulink and deployed into the PX4 autopilot hardware. The high-fidelity model built by ADAMS communicates with PX4 through Simulink.

This part builds a hardware-in-the-loop(HIL) platform with the robot's high-fidelity model and PX4 autopilot hardware. HIL experiments are effective methods that can be used to test embedded control systems efficiently. The robot's model was established in ADAMS and Matlab/Simulink with detailed parameters. The connection of the HIL platform designed in this work is shown in Fig.11. We used a normal controller with parallel cascade PID modules to verify the robustness and effectiveness of the proposed controller.

Fig.12 to Fig.16 are comparative results of control effects. We compared the proposed controller with the normal con-

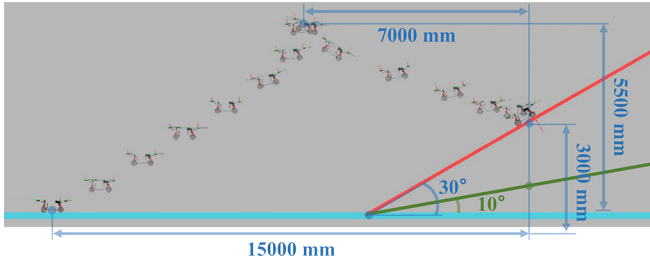


Fig. 12. Simulation environment and motion trajectories in a 10° and 30° scenes.

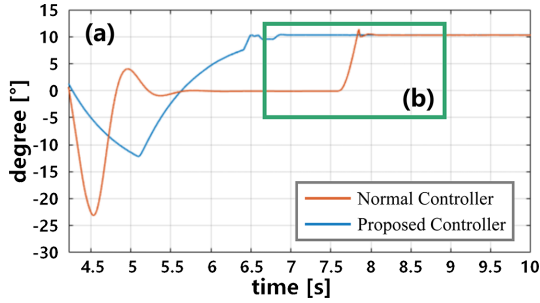


Fig. 13. Variation trend of robot's pitch angle in a 10° scene. (a) The pitch angle changes from hovering to landing. (b) The view of the landing moment.

troller with the waypoint and conducted experimental verification in 10° and 30° slope scenarios. Fig.12 denotes the robot's experimental setup and flight trajectory. To further describe the optimization of the proposed controller for the slope mode switching of the land-air robot. We also characterize it by pitch angle, velocity, and spring travel, as shown in Fig.13 to Fig.15.

The trends of pitch angles during the landing tasks are shown in Fig.13 and Fig.14. The proposed controller can adjust robot's pitch angle to be consistent with the slope before landing. Meanwhile, the robot will not fly backward or oscillate by leaning back. Furthermore, the views in green rectangle are the oscillation of the pitch angle at the moment of landing, indicating whether the robot's landing is smooth. When the robot with proposed controller landed in the 10° scene, it remained stable almost instantly. However, the normal controller has a pitch angle of 2° oscillation in this scene. In the 30° scene, the proposed controller is still quickly stable within 0.2s after landing, and the maximum pitch angle is about 2.5°. The maximum oscillation angle of the normal controller exceeds 4°, and after two oscillations, it tends to stabilize after about 0.5s after landing. Fig.15 shows the velocity curves that perpendicular to the direction of the descent slope. Similar to the pitch angle, it also characterizes the smooth of the robot when landing. Finally, Fig.15 shows the suspension strokes that reflect the magnitude of the impact force when landing intuitively. In the 10° scene task, the suspension stroke of the robot with the proposed controller is about 34.3% less than with the normal controller. Moreover, the suspension convergence time is 0.12s and 0.31s, respectively. In the 30° scene task, the suspension stroke of the robot with the proposed controller is about 21.7% less than with the normal controller. The suspension time is 0.28s and 0.44s, respectively.

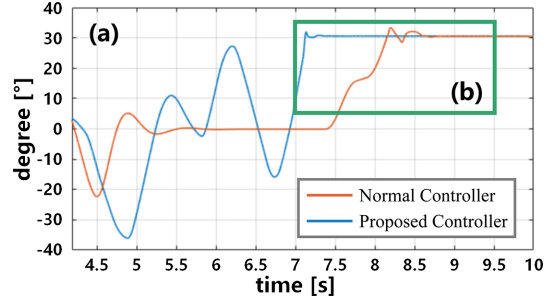


Fig. 14. Variation trend of robot's pitch angle in a 10° scene. (a) The pitch angle changes from hovering to landing. (b) The view of the landing moment

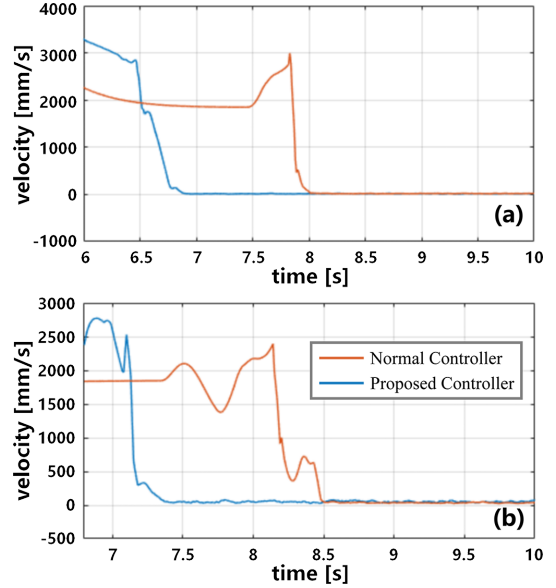


Fig. 15. Variation trend of robot's velocity. (a) 10° scene. (b) 30° scene.

Furthermore, we measured the landing speed of the robot when only perturbed by ground effects. In the 10° slope descent task, the normal and proposed controllers take 3.77 s and 3.3 s to land, respectively, getting 14.2% increases the speed. In the 30° slope landing task, the normal controller takes 3.98 s to land, the proposed controller takes 3 s to land, and 32.7% increases the speed. To verify the controller robustness, we add forces of 0 N to 40 N, 60 N, and 80 N at the robot center of mass to simulate external disturbances. The directions and magnitudes of these disturbance forces are randomly generated. In this setting, the robot performed 10 experiments with different controllers in each of the two scenarios. We characterized the landing accuracy by mean-variance of the landing offsets between the actual landing point and the expected landing point, as shown in Tab.II. Under random disturbance, the proposed controller has a noticeable improvement in speed and landing accuracy compared with the normal controller.

VI. CONCLUSION

The multi-modal motion mode effectively improves the motion capability and practicability of the robot. This paper introduced a deformable robot with land-air motion and

TABLE II
THE UNDISTURBED LANDING TIME IS OFFSET FROM THE ROBOT LANDING POINT WITH RANDOM DISTURBANCE.

Controller	Landing Time	Offset (40 N)	Offset (60 N)	Offset (80 N)	Mean Variance
Proposed Controller (10°)	3.30 s	282.99 mm	343.60 mm	243.15 mm	292.84 mm
Normal Controller (10°)	3.77 s	468.76 mm	500.81 mm	576.72 mm	517.41 mm
Proposed Controller (30°)	3.00 s	229.30 mm	220.00 mm	372.27 mm	282.59 mm
Normal Controller (30°)	3.98 s	391.40 mm	339.26 mm	488.07 mm	410.89 mm

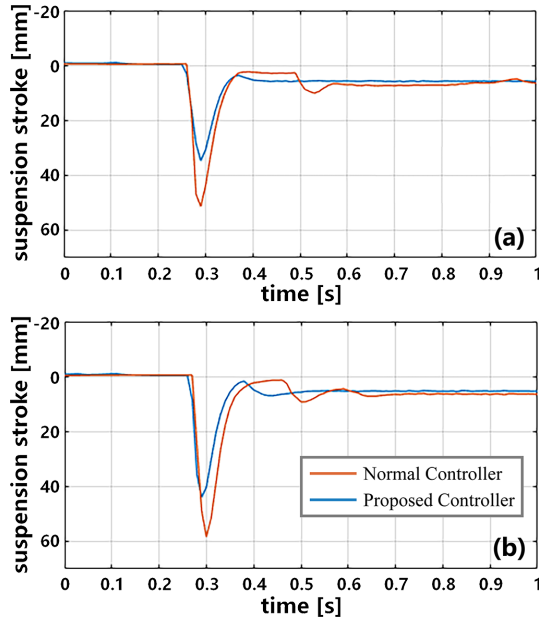


Fig. 16. Variation trend of robot's suspension strokes. (a) 10° scene. (b) 30° scene.

continuous switching capability, and established its detailed coupled dynamics model. A fusion controller based on JLT and LQR is designed to focus on the unstructured scene and land-air switching motion. The controller considered the robot's control assignment, land-air actuators, and ground-effect disturbance, which enabled the robot to achieve fast and robust mode switching. Combined with the coupled dynamics model and the proposed fusion controller, we build a hardware-in-the-loop system for a high-fidelity robot model based on ADAMS/Simulink. The robot has conducted ground driving and mode-switching experiments in the hardware-in-the-loop system and practice. The results show that the deformable structures effectively improved the ground-driving accuracy of the robot. Compared with the normal controller, the proposed controller can significantly improve the robot's trajectory planning, speed, and mode-switching flexibility in the slope scenes.

VII. ACKNOWLEDGMENT

This work was supported by the National High Technology Research and Development Program of China under Grant No. 2018YFE0204300, the National Natural Science Foundation of China under Grant No. 62273198, U1964203.

REFERENCES

- [1] S. Martínez-Rozas, R. Rey, D. Alejo, D. Acedo, J. A. Cobano, A. Rodríguez-Ramos, P. Campoy, L. Merino, and F. Caballero, "An aerial/ground robot team for autonomous firefighting in urban gnss-denied scenarios," 2022.
- [2] C. Zhao, P. R. Thies, and L. Johanning, "Offshore inspection mission modelling for an asv/rov system," *Ocean Engineering*, vol. 259, p. 111899, 2022.
- [3] D. D. Fan, R. Thakker, T. Bartlett, M. B. Miled, L. Kim, E. Theodorou, and A.-a. Agha-mohammadi, "Autonomous Hybrid Ground/Aerial Mobility in Unknown Environments," in *2019 IEEE/RSJ International Conference on Intelligent Robots and Systems (IROS)*. IEEE, nov 2019, pp. 3070–3077.
- [4] A. Kalantari and M. Spenko, "Modeling and performance assessment of the HyTAQ, a hybrid terrestrial/aerial quadrotor," *IEEE Transactions on Robotics*, vol. 30, no. 5, pp. 1278–1285, 2014.
- [5] C. J. Dudley, A. C. Woods, and K. K. Leang, "A micro spherical rolling and flying robot," *IEEE International Conference on Intelligent Robots and Systems*, vol. 2015-Decem, pp. 5863–5869, 2015.
- [6] S. Wen, J. Han, Z. Ning, Y. Lan, X. Yin, J. Zhang, and Y. Ge, "Numerical analysis and validation of spray distributions disturbed by quad-rotor drone wake at different flight speeds," *Computers and Electronics in Agriculture*, vol. 166, p. 105036, 2019.
- [7] Q. Tan, X. Zhang, H. Liu, S. Jiao, M. Zhou, and J. Li, "Multi-modal dynamics analysis and control for amphibious fly-drive vehicle," *IEEE/ASME Transactions on Mechatronics*, vol. 26, no. 2, pp. 621–632, 2021.
- [8] P. Ratsamee, P. Kriengkamol, T. Arai, K. Kamiyama, Y. Mae, K. Kiyokawa, T. Mashita, Y. Uranishi, and H. Takemura, "A hybrid flying and walking robot for steel bridge inspection," *SSRR 2016 - International Symposium on Safety, Security and Rescue Robotics*, pp. 62–67, 2016.
- [9] A. Kalantari, T. Touma, L. Kim, R. Jitosh, K. Strickland, B. T. Lopez, and A. A. Agha-Mohammadi, "Drivocopter: A concept Hybrid Aerial/Ground vehicle for long-endurance mobility," *IEEE Aerospace Conference Proceedings*, 2020.
- [10] Q. Tan, X. Zhang, H. Liu, S. Jiao, M. Zhou, and J. Li, "Multi-modal dynamics analysis and control for amphibious fly-drive vehicle," *IEEE/ASME Transactions on Mechatronics*, vol. 26, no. 2, pp. 621–632, 2021.
- [11] J. Hu, Y. Liang, and X. Diao, "A flying-insect-inspired hybrid robot for disaster exploration," *2017 IEEE International Conference on Robotics and Biomimetics, ROBIO 2017*, vol. 2018-Janua, pp. 270–275, 2018.
- [12] A. Sharif, S. Choi, and H. Roth, "A new algorithm for autonomous outdoor navigation of robots that can fly and drive," *ACM International Conference Proceeding Series*, vol. Part F1476, pp. 141–145, 2019.
- [13] N. Meiri and D. Zarrouk, "Flying STAR, a hybrid crawling and flying sprawl tuned robot," *Proceedings - IEEE International Conference on Robotics and Automation*, vol. 2019-May, pp. 5302–5308, 2019.
- [14] A. Kossett, R. D'Sa, J. Purvey, and N. Papanikolopoulos, "Design of an improved land/air miniature robot," *Proceedings - IEEE International Conference on Robotics and Automation*, pp. 632–637, 2010.
- [15] H. Wang, J. Shi, J. Wang, H. Wang, Y. Feng, and Y. You, "Design and modeling of a novel transformable land/air robot," *International Journal of Aerospace Engineering*, vol. 2019, 2019.
- [16] P. Ramon-Soria, A. E. Gomez-Tamm, F. J. Garcia-Rubiales, B. C. Arrue, and A. Ollero, "Autonomous landing on pipes using soft gripper for inspection and maintenance in outdoor environments," in *2019 IEEE/RSJ International Conference on Intelligent Robots and Systems (IROS)*. IEEE, 2019, pp. 5832–5839.
- [17] K. Zhang, Y. Shi, and H. Sheng, "Robust nonlinear model predictive control based visual servoing of quadrotor uavs," *IEEE/ASME Transactions on Mechatronics*, vol. 26, no. 2, pp. 700–708, 2021.

- [18] S. Lee, T. Shim, S. Kim, J. Park, K. Hong, and H. Bang, "Vision-based autonomous landing of a multi-copter unmanned aerial vehicle using reinforcement learning," in *2018 International Conference on Unmanned Aircraft Systems (ICUAS)*. IEEE, 2018, pp. 108–114.
- [19] X. Zhou, Z. Wang, H. Ye, C. Xu, and F. Gao, "Ego-planner: An esdf-free gradient-based local planner for quadrotors," *IEEE Robotics and Automation Letters*, vol. 6, no. 2, pp. 478–485, 2020.
- [20] A. Paris, B. T. Lopez, and J. P. How, "Dynamic landing of an autonomous quadrotor on a moving platform in turbulent wind conditions," in *2020 IEEE International Conference on Robotics and Automation (ICRA)*. IEEE, 2020, pp. 9577–9583.
- [21] X. Zhang, J. Huang, Y. Huang, K. Huang, L. Yang, Y. Han, L. Wang, H. Liu, J. Luo, and J. Li, "Intelligent amphibious ground-aerial vehicles: State of the art technology for future transportation," *IEEE Transactions on Intelligent Vehicles*, 2022.
- [22] X. Zhang, Y. Huang, K. Huang, X. Wang, D. Jin, H. Liu, and J. Li, "A multi-modal deformable land-air robot for complex environments," *arXiv preprint arXiv:2210.16875*, 2022.
- [23] W. Saab, W. S. Rone, and P. Ben-Tzvi, "Robotic tails: a state-of-the-art review," *Robotica*, vol. 36, no. 9, pp. 1263–1277, 2018.
- [24] R. Moreno, F. Veenstra, D. Silvera, J. Franco, O. Gracia, E. Cordoba, J. Gomez, and A. Faina, "Automated reconfiguration of modular robots using robot manipulators," in *2018 IEEE Symposium Series on Computational Intelligence (SSCI)*. IEEE, 2018, pp. 884–891.
- [25] F. Chen, R. Jiang, K. Zhang, B. Jiang, and G. Tao, "Robust backstepping sliding-mode control and observer-based fault estimation for a quadrotor uav," *IEEE Transactions on Industrial Electronics*, vol. 63, no. 8, pp. 5044–5056, 2016.
- [26] D. Falanga, K. Kleber, S. Mintchev, D. Floreano, and D. Scaramuzza, "The foldable drone: A morphing quadrotor that can squeeze and fly," *IEEE Robotics and Automation Letters*, vol. 4, no. 2, pp. 209–216, 2018.
- [27] H. B. Pacejka and E. Bakker, "The magic formula tyre model," *Vehicle system dynamics*, vol. 21, no. S1, pp. 1–18, 1992.
- [28] M. Hehn and R. D'Andrea, "Quadcopter trajectory generation and control," *IFAC proceedings Volumes*, vol. 44, no. 1, pp. 1485–1491, 2011.
- [29] M. W. Mueller, M. Hehn, and R. D'Andrea, "A computationally efficient motion primitive for quadcopter trajectory generation," *IEEE transactions on robotics*, vol. 31, no. 6, pp. 1294–1310, 2015.
- [30] C. Paz, E. Suárez, C. Gil, and C. Baker, "Cfd analysis of the aerodynamic effects on the stability of the flight of a quadcopter uav in the proximity of walls and ground," *Journal of Wind Engineering and Industrial Aerodynamics*, vol. 206, p. 104378, 2020.
- [31] X. Kan, J. Thomas, H. Teng, H. G. Tanner, V. Kumar, and K. Karydis, "Analysis of ground effect for small-scale uavs in forward flight," *IEEE Robotics and Automation Letters*, vol. 4, no. 4, pp. 3860–3867, 2019.
- [32] I. C. Cheeseman and W. E. Bennett, *The Effect of the Ground on a Helicopter Rotor in Forward Flight*, 1955, vol. 3021, no. 3021. [Online]. Available: <https://reports.aerade.cranfield.ac.uk/handle/1826.2/3590>
- [33] J. Liao, Z. Chen, and B. Yao, "Model-based coordinated control of four-wheel independently driven skid steer mobile robot with wheel-ground interaction and wheel dynamics," *IEEE Transactions on Industrial Informatics*, vol. 15, no. 3, pp. 1742–1752, 2018.



Xinyu Zhang was born in Huining, Gansu Province, and he received a B.E. degree from the School of Vehicle and Mobility at Tsinghua University, in 2001. He was a visiting scholar at the University of Cambridge.

He is currently a researcher with the School of Vehicle and Mobility, and the head of the Mengshi Intelligent Vehicle Team at Tsinghua University. Dr. Zhang is the author of more than 30 SCI/EI articles. His research interests include intelligent driving and multimodal information fusion.



Yuanhao Huang was born in Chengdu, Sichuan Province, and he received the B.E. degree from the Institute of Disaster Prevention Department, Beijing, China, in 2020. Now he is pursuing a Master degree in engineering at Inner Mongolia University of Technology, Hohhot, China. He is currently working on a joint training program at New Technology Concept Automobile Research Institute, Tsinghua University. His research interests include robotics, automatic control and SLAM.



Kangyao Huang received the B.Eng. degree in Aerospace from Northwestern Polytechnical University, Xi'an, China, in 2016, and the M.Res. degree in Control & Systems Engineering from the University of Sheffield, Sheffield, U.K., in 2020. Currently he is pursuing a Ph.D degree at the Department of Computer Science and Technology, Tsinghua University, Beijing, China, and working with the Mengshi Intelligent Vehicle Team.

He has three years working experience in aerospace industry. He was the Founder, Technical Director and Chief Engineer with Bingo Intelligence Aviation Technology co., LTD, where he developed the general software architecture for integrated avionics system, and provided applied research in cooperation with partners in aerospace and manufacturing sectors. His research interests include swarm robotics, UAV engineering, and embodied intelligence.



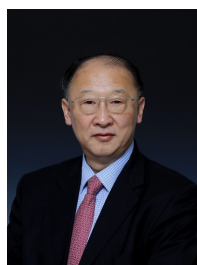
Ziqi Zhao was born in Tongren, Guizhou province. Now he is studying for a Bachelor's degree in Engineering at the Institute of Disaster Prevention Science and Technology. He is currently doing a research internship at Tsinghua University. His research interests include robotics, automatic control and SLAM and Navigation2.



Jingwei Li was born in Jinghe, Xinjiang Province, and he received the B.E. degree from the College of Mechanical and Electronic Control Engineering at the Beijing Jiaotong University, in 2021. Now he is pursuing a Master degree in engineering at Beijing University of Aeronautics and Astronautics. He has assisted in completing the simulation task of the Institute. His research interests include automatic control and analog simulation.



Huaping Liu (Senior Member, IEEE) is an Associate Professor with the Department of Computer Science and Technology, Tsinghua University, Beijing, China. His research interests include robot perception and learning. Dr. Liu has served as an Associate Editor of ICRA and IROS and in the Program Committees of IJCAI, RSS, and IJCNN. He is an Associate Editor of the IEEE ROBOTICS AND AUTOMATION LETTERS, Neurocomputing, and Cognitive Computation.



Jun Li (Fellow, Chinese Academy of Engineering) received the Ph.D. degree in internal combustion engineering from Jilin Polytechnic University, Changchun, China, in 1989. He is a fellow of the Chinese Academy of Engineering, and the Vice-Chief Engineer and the Director of the Research and Development Center with China FAW Group Corporation, Changchun.